Magnetic model in multiferroic $NdFe_3(BO_3)_4$ investigated by inelastic neutron scattering

S. Hayashida,[1] M. Soda,[1] S. Itoh,[2] T. Yokoo,[2] K. Ohgushi,[3] D. Kawana,[1] H. M. Rønnow,[1,4] and T. Masuda[1]

[1]*Neutron Science Laboratory, Institute for Solid State Physics, University of Tokyo, Tokai, Ibaraki 319-1106, Japan*

[2]*Neutron Science Division, Institute of Materials Structure Science, High Energy Accelerator Research Organization, Tsukuba, Ibaraki 305-0801, Japan*

[3]*Department of Physics, Tohoku University, Sendai, Miyagi 980-8581, Japan*

[4]*Laboratory for Quantum Magnetism, École Polytechnique Fédérale Lausanne (EPFL), CH-1015 Lausanne, Switzerland*

(Received 30 May 2015; published 4 August 2015)

We performed inelastic neutron scattering measurements on single crystals of $NdFe_3(^{11}BO_3)_4$ to explore the magnetic excitations, to establish the underlying Hamiltonian, and to reveal the detailed nature of hybridization between the $4f$ and $3d$ magnetism. The observed spectra exhibiting a couple of key features, i.e., anticrossing of Nd and Fe excitations and anisotropy gap at the antiferromagnetic zone center, are explained by the magnetic model including spin interaction in the framework of weakly coupled Fe^{3+} chains, interaction between the Fe^{3+} and Nd^{3+} moments, and single-ion anisotropy derived from the Nd^{3+} crystal field. The combination of the measurements and calculations reveals that the hybridization between $4f$ and $3d$ magnetism propagates the local magnetic anisotropy of the Nd^{3+} moment to the Fe^{3+} network, leading to the determination of the bulk structure of both electric polarization and magnetic moment in the multiferroics of the spin-dependent metal-ligand hybridization type.

DOI: 10.1103/PhysRevB.92.054402 PACS number(s): 75.10.Dg, 75.25.−j, 75.85.+t

I. INTRODUCTION

Coexistence of magnetic order and electric polarization, multiferroicity, has become a major topic over the past decade in condensed matter physics. Since multiferroicity was originally discovered in perovskite $TbMnO_3$ [1], various multiferroic compounds have been found, including $RMnO_3$ (R = Eu, Gd, Tb, and Dy) [2], $Ba_{0.5}Sr_{1.5}Zn_2Fe_{12}O_{22}$ [3], $Ni_3V_2O_8$ [4], $CoCr_2O_4$ [5], $MnWO_4$ [6], $CuFeO_2$ [7], $LiCu_2O_2$ [8], $LiCuVO_4$ [9], and $Ba_2CoGe_2O_7$ [10]. Recent theoretical and experimental studies revealed that the electric polarization in these compounds is driven by magnetic long-range order [11–15]. Since the structure of the order is determined by the exchange pathways and the magnetic anisotropy, experimental identification of the magnetic Hamiltonian is very important for understanding multiferroics.

The rare-earth ferroborates $RFe_3(BO_3)_4$ (R = rare-earth metal) are a series of new multiferroic compounds containing R^{3+} ($4f^n$) and Fe^{3+} ($3d^5$ $S = 5/2$) as magnetic ions. The variety of the magnetic anisotropy of the R^{3+} moments (R = Y, Pr, Nd, Sm, Gd, and Tb) combined with the interaction between the Fe^{3+} and R^{3+} moments (f-d coupling) gives rise to diverse magnetoelectric (ME) effects as a function of the R^{3+} ions [16–21]. In these compounds the mechanism of magnetoelectricity is explained by the spin-dependent metal-ligand hybridization model [22,23].

The crystal structure has the trigonal space group $R32$, which belongs to the structural type of the mineral huntite $CaMg_3(CO_3)_4$ [24]. As shown in Fig. 1(a) the main feature is that distorted FeO_6 octahedra form spiral chains with threefold screw-axis symmetry along the crystallographic c axis. Each chain includes three Fe^{3+} ions in the unit cell. The chains are separated by the R^{3+} and B^{3+} ions.

In $NdFe_3(BO_3)_4$ the Nd^{3+} ions ($4f^3$) carry magnetic moment with $J = 9/2$. The magnetic susceptibility showed anisotropic decrease below 29 K, and the heat capacity showed well-defined λ type anomaly at the same temperature, implying a phase transition to an antiferromagnetic (AF) ordered state with Néel temperature of $T_N = 29$ K [25]. At $T \geqslant T_N$ the susceptibility is concave downward, indicating the short-range AF order because of the low dimensionality of the magnetic system. Spontaneous electric polarization simultaneously appears in the AF ordered phase [20]. The electric polarization significantly increases upon applying a magnetic field parallel to the a axis. The magnitude of the electric polarization reaches $P_a \sim 300\ \mu C/m^2$ at 1.3 T and 4.2 K [17,18], which means that the magnetization along the a axis induces the large electric polarization along the a axis. A neutron diffraction study exhibited an easy-plane-type AF order at $T \leqslant T_N$; the Fe^{3+} and Nd^{3+} magnetic moments align ferromagnetically along the a axis and propagate antiferromagnetically along the c axis with the propagation vector $\boldsymbol{k} = (0, 0, 3/2)$ in Fig. 1(a) [26,27]. Both of Fe^{3+} and Nd^{3+} moments are simultaneously ordered at the T_N, indicating non-negligible f-d coupling. Further decreasing the temperature at $T \leqslant T_{IC} = 13.5$ K, the commensurate (C) magnetic peak splits into a pair of incommensurate (IC) peaks where the magnetic moments are in the ab plane and the AF helix propagates along the c axis.

Magnetic dynamics have been investigated by spectroscopic methods using electromagnetic waves. ESR measurement detected an energy gap suggesting a uniaxial magnetic anisotropy in the ab plane [28]. It also detected lifting of the Kramers doublet of the Nd^{3+} ion due to the molecular field from the neighboring Fe^{3+} ions. Optical spectroscopy provided the energy levels of the crystal field of the Nd^{3+} ion and determined the parameters of the crystal field Hamiltonian [29].

In $NdFe_3(BO_3)_4$ exhibiting the strong f-d coupling, the investigation of excitation spectra including Fe^{3+} spin wave and Nd^{3+} crystal field in a wide wave-vector energy space is crucial in order to identify the magnetic Hamiltonian and to unravel the detailed nature of hybridization between $3d$ and $4f$ magnetism. Furthermore in constructing the Hamiltonian,

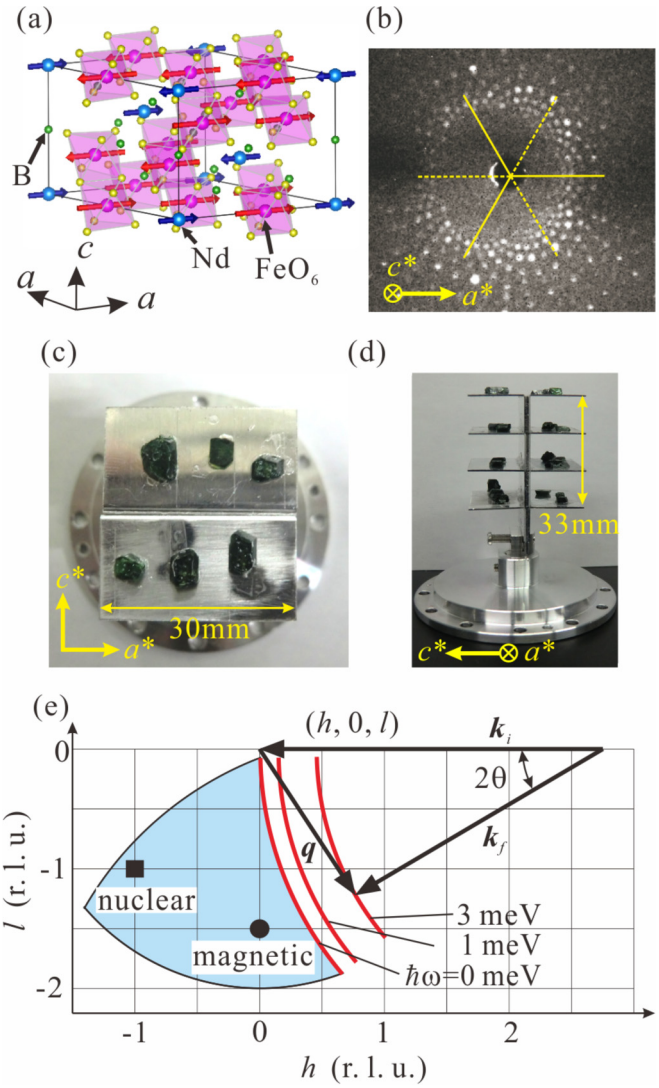

FIG. 1. (Color online) (a) The crystal structure and magnetic structure of $NdFe_3(BO_3)_4$ (hexagonal, space-group $R32$). (b) Laue image of a crystal with the c^* axis parallel to the incident x-ray beam. Crystals of $NdFe_3(^{11}BO_3)_4$ on the alumina holder viewed from above (c) and from the side (d). (e) Reciprocal space in the a^*-c^* plane. The square at $(h,k,l) = (-1,0,-1)$ is a nuclear Bragg reflection. The circle at $(0,0,-1.5)$ is a magnetic Bragg reflection. Red curves indicate spectra measured with $\boldsymbol{k}_i // a^*$ for $\hbar\omega = 0,1$ and 3 meV. The blue shaded area indicates the range of the observed scattering plane for $k_i = 2.352$ Å^{-1} and $\hbar\omega = 0$ meV when sample is rotated.

careful consideration of magnetic anisotropy is important in the multiferroics of the spin-dependent metal-ligand hybridization mechanism type [14,15], in which the magnetic anisotropy directly determines the polarization structure.

In the present paper we study inelastic neutron scattering (INS) spectra on $NdFe_3(^{11}BO_3)_4$ to explore the magnetic excitations and to establish the underlying Hamiltonian. Following to the introduction we describe the experimental details about the sample preparation and the setup of INS measurements in Sec. II. Subsequently in Sec. III the INS spectra of $NdFe_3(^{11}BO_3)_4$ are demonstrated. We observed spin waves of the Fe^{3+} moment below 6 meV and transition between the lifted states of Kramers doublet of the Nd^{3+} ion at 1 meV. A couple of characteristic features are an anticrossing of the Fe and Nd excitations, and a small anisotropy gap at the antiferromagnetic zone center. In Sec. IV the magnetic model including an in-plane anisotropy derived from the crystal field excitation of the Nd^{3+} moment and the non-negligible f-d coupling is constructed. The observed spectra are successfully analyzed by the linear spin-wave theory based on the model. The origin of the in-plane anisotropy is revealed to be the crystal field of the Nd^{3+} ion. In Sec. V possibility of magnetic anisotropy of the Fe^{3+} moment is discussed. It is turned out that the anisotropy is very small, and, instead, the Fe^{3+} moment inherits an in-plane anisotropy through hybridization with the Nd^{3+} moment. The conclusions are given in Sec. VI. The magnetic Hamiltonian in $NdFe_3(^{11}BO_3)_4$ is established in the present study. Combination of the measurement and the detailed calculation revealed that the hybridization between $4f$ and $3d$ magnetism propagates the local magnetic anisotropy of the Nd^{3+} ion to the Fe^{3+} network, resulting in the bulk structure of multiferroics. The local symmetry of the rare-earth ion is a driving force for the nonlocal multiferroicity in $NdFe_3(^{11}BO_3)_4$.

II. EXPERIMENTAL DETAILS

Single crystals of $NdFe_3(^{11}BO_3)_4$ were grown by a flux method [30]. We first synthesized polycrystalline samples from the starting materials, Nd_2O_3, Fe_2O_3, and $^{11}B_2O_3$. The stoichiometric amounts of the starting materials with a total mass of about 16 g were mixed, ground, and put into an alumina crucible. The crucible was heated at 980 °C for 72 h. The flux is $Bi_2Mo_3O_{12} + 3\,^{11}B_2O_3 + 3/5\ Nd_2O_3$; $Bi_2Mo_3O_{12}$ was synthesized by the solid-state reaction from Bi_2O_3 and MoO_3 inside an alumina crucible at 600 °C for 24 h. A mixture of about 60 g of $NdFe_3(^{11}BO_3)_4$ and the flux with the mass ratio of 1 : 3 was put into a platinum crucible inside the alumina crucible. The crucible was heated to 1000 °C for 4 h, kept at this temperature for 1 h, cooled to 962 °C for 1 h, and slowly cooled down to 870 °C for 120 h; then the furnace was shut down to the room temperature. The flux was removed by decanting at 900 °C, and washing the crystals with HCl solutions.

We coaligned 22 pieces of single crystals so that the crystallographic a^*-c^* plane is horizontal. Alignment was performed by transmission Laue method using a high-energy x-ray Laue camera. The x-ray source was YXLON MG452 and the maximum energy of the white x-ray beam was 310 keV. We recorded Laue patterns using a high-speed CCD camera, with imaging size 10 cm × 10 cm (1024 × 1024 pixel). Figure 1(b) shows a Laue image of a crystal in the c^* plane. This pattern exhibits the threefold symmetry along the c^* axis. We placed the crystals on an alumina holder as shown in Figs. 1(c) and 1(d). The average mass of the crystals was 0.1 g. The total mass of the sample was 2.1 g.

The INS experiment was performed at the High Resolution Chopper Spectrometer (HRC) installed in the Material and Life Science Experimental Facility of J-PARC [31–33]. At the HRC white neutrons are monochromatized by a Fermi chopper synchronized with the production timing of the pulsed neutrons. The energy transfer $\hbar\omega$ was determined from the time of flight (TOF) of the scattered neutrons detected at position

sensitive detectors (PSDs). The T_0 chopper was set at 50 Hz, a collimator of 1.5° was installed in front of the sample, and the "S" Fermi chopper with 200 Hz was used to obtain high neutron flux. We used a GM-type closed cycle cryostat to achieve 41 K and 15 K. The energy of the incident neutron beam was $E_i = 11.46$ meV yielding an energy resolution of $\Delta E = 0.3$ meV at the elastic position.

Figure 1(e) illustrates the a^*-c^* scattering plane. Reciprocal lattice positions at $\boldsymbol{q} = (-1,0,-1)$ and $(0,0,-1.5)$ are the positions of nuclear and magnetic Bragg peaks, respectively. Throughout this paper $\boldsymbol{q}$ is expressed in reciprocal lattice unit, $\boldsymbol{q} = (h,k,l)$. INS spectra with $\boldsymbol{k}_i // a^*$ were measured at 41 K and 15 K. Red curves in Fig. 1(e) indicate the measured $\boldsymbol{q}$ ranges for $\hbar\omega = 0,1$ and 3 meV. At 15 K INS spectra that cover wide $\boldsymbol{q}$ range were measured by rotating the crystal by 70 degrees in two-degree steps. The $\boldsymbol{q}$ range in the scan for $\hbar\omega = 0$ meV is indicated by the blue shaded area in Fig. 1(e). The range of out of plane momentum is $|q_\perp| < 0.41$ Å^{-1}. In the following, the out of plane spectra are integrated in the central range $|q_\perp| < 0.13$ Å^{-1}, and we show all spectra in the $(h,0,l)$ plane.

III. EXPERIMENTAL RESULTS

The INS spectra projected onto the c^* axis at 41 K and 15 K are shown in Figs. 2(a) and 2(b), respectively. At 41 K a diffuse spectrum of paramagnetic scattering emerges from $l = -1.5$. At 15 K dispersive excitations emerge in the energy range of 2.5 meV $< \hbar\omega <$ 4.5 meV, which is interpreted as spin waves of the Fe^{3+} moments.

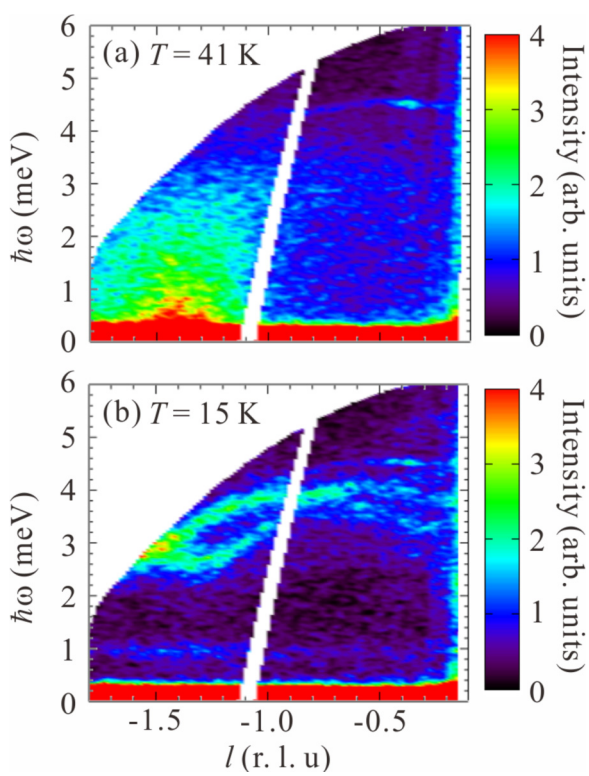

FIG. 2. (Color online) Inelastic neutron spectra projected onto c^* axis at (a) 41 K and (b) 15 K. The incident neutron energy was 11.46 meV.

Figures 3(a)–3(d) display neutron spectra at 15 K sliced at the energies of 0, 1, 2, and 3 meV in the a^*-c^* plane. The white arcs are because of the absence of the neutron detectors between the detector banks. In Fig. 3(a) the peak at $\boldsymbol{q} = (-1,0,-1)$ is a nuclear Bragg reflection, and the peak at $(0,0,-1.5)$ is a magnetic Bragg reflection. The peaks at other $\boldsymbol{q}$s are not identified; they may be Bragg reflections from minor grains of crystals. The rings expanding from $(0,0,-1.5)$ in Figs. 3(b)–3(d) imply that a dispersive excitation appears from $(0,0,-1.5)$. The rings are flattened along the c^* axis, which means that the dispersion along the c^* axis is steeper than that along the a^* axis. This is consistent with the naive prediction from the crystal structure that the intrachain interaction along the c axis is strong compared with the interchain interaction.

The INS spectrum at 15 K projected onto the $\hbar\omega$-$(0,0,l)$ plane by the integrating the neutron intensity in the ranges of $-0.1a^* \leqslant q \leqslant 0.1a^*$ along the $\boldsymbol{a}^*$ direction in the scattering plane and $-0.17a^* \leqslant q \leqslant 0.17a^*$ perpendicular to the scattering plane is shown in Fig. 4(a). The spectrum projected onto $\hbar\omega$-$(h,0,-1.5)$ plane by the integration in the ranges of $-0.17a^* \leqslant q \leqslant 0.17a^*$ perpendicular to the scattering plane and $-1.6c^* \leqslant q \leqslant -1.4c^*$ along the $\boldsymbol{c}^*$ direction is shown in Fig. 4(b). We clearly observed the spin waves of the Fe^{3+} moments around $\boldsymbol{q} = (0,0,-1.5)$, and the flat excitation at about 1.0 meV, which is the transition between the lifted states of Kramers doublet of the Nd^{3+} ion. The spin waves of the Fe^{3+} moments are more dispersive along the c^* direction than along the a^* direction, which is consistent with the flattened ring in Figs. 3(b)–3(d).

A series of $\hbar\omega$ dependence of the neutron intensity obtained by the integration in the same $\boldsymbol{q}$ ranges that were used for the display of Figs. 4(a) and 4(b) were fitted by Gaussian functions to investigate the detailed structures of the excitations. The peak energies were plotted as open circles in Figs. 4(a) and 4(b). These data will be used in the analysis section. The white circles around $\boldsymbol{q} = (0,0,-1.5)$ exhibit an anticrossing between the spin wave of the Fe^{3+} moments and the flat mode of the Nd^{3+} moments, meaning that the Fe^{3+} moments interact with the Nd^{3+} moments.

Figure 5(a) shows the $\hbar\omega$ dependence of the neutron intensity obtained by the integration in the $\boldsymbol{q}$ range of $h = [-0.5,0]$ and $l = [-1,-0.7]$, where the Nd^{3+}-based mode is not affected by the Fe^{3+}-based spin-wave mode. The dashed curve is incoherent elastic scattering and the blue curve is a Gaussian fit. The red curve is the sum of the dashed and blue curves. The gray shaded area is the energy resolution. From the peak position we identify the magnitude of the energy split of the Kramers doublet to be 0.98 meV. Figure 5(b) shows a constant-$\boldsymbol{q}$ scan at $(0,0,-1.5)$, the AF zone center, which is obtained by integration in the $\boldsymbol{q}$ range of $h = [-0.1,0.1]$ and $l = [-1.6,-1.4]$. The dashed curve is incoherent elastic scattering, the blue curves are Gaussian fits, and the red curve is the sum of the dashed and blue curves. The gray shaded areas indicate the energy resolutions. The magnitude of the energy gap at the AF zone center is estimated as 0.57 meV. The gap implies the existence of an anisotropy in the ab plane. The excitation at 1.3 meV is the transition between the split of Kramers doublet of the Nd^{3+} ion. The peak energies of the Nd^{3+} ion in Figs. 5(a) and 5(b) are obviously different. The energy difference is due to the hybridization

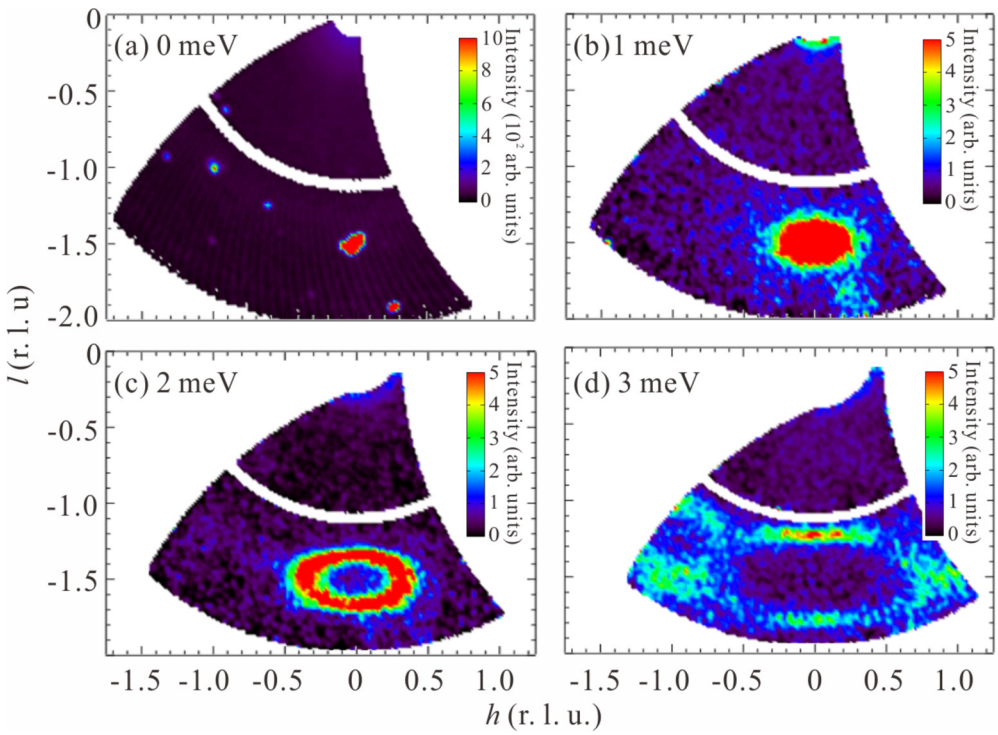

FIG. 3. (Color online) Constant energy cuts at (a) 0 meV, (b) 1 meV, (c) 2 meV, and (d) 3 meV in the a^*-c^* plane. The horizontal and vertical axes represent the a^* and c^* axes, respectively

between the Fe^{3+} and Nd^{3+} modes. The energy widths of the excitations at $\hbar\omega = 0.57$ meV and 1.3 meV are broader than the experimental resolution. The energy split of 0.98 meV and the energy gap of 0.57 meV are consistent with the magnetic excitations reported from ESR measurement [28] and optical spectroscopy [29].

IV. ANALYSIS

In order to identify the magnetic model realized in $NdFe_3(^{11}BO_3)_4$, we consider the following Hamiltonian:

$$\mathcal{H} = -\sum_{\text{n.n.}} J_1 \boldsymbol{S}_i \cdot \boldsymbol{S}_j - \sum_{\text{n.n.n.}} J_2 \boldsymbol{S}_i \cdot \boldsymbol{S}_j - \sum_{\text{n.n.}} J_3 \boldsymbol{S}_i \cdot \boldsymbol{J}_k + \sum_k \mathcal{H}_{\text{CF}}(\boldsymbol{J}_k), \quad (1)$$

where the x axis is parallel to the crystallographic a axis and the z axis is parallel to the c axis. J_1 and J_2 are the exchange interactions in the nearest- and second-nearest-neighbor paths of the Fe^{3+} ions as shown in Figs. 6(a) and 6(b). These terms mainly determine the dispersions along the c^* axis and a^* axis, respectively. J_3 is the nearest-neighbor exchange interaction between the Fe^{3+} and Nd^{3+} moments, which induces the anticrossing between the Fe^{3+} and Nd^{3+} modes. In Eq. (1), positive (negative) signs of the exchange parameters correspond to ferromagnetic (antiferromagnetic) exchange interactions. $\mathcal{H}_{\text{CF}}$ is the crystal field Hamiltonian of the Nd^{3+} ion.

There are five Kramers doublets in the crystal field of the Nd^{3+} ion above $T_N = 30$ K. The first excited energy is about 8 meV, and the second one is about 17 meV as reported in Ref. [29]. In the calculation of the low-energy excitations below 6 meV it is assumed that only the ground state in the crystal field of the Nd^{3+} ion hybridizes with the Fe^{3+} moments. For this assumption, we introduce the ground state of the crystal field of the Nd^{3+} ion.

At the Nd^{3+} site with D_3 symmetry, the crystal field Hamiltonian can be defined as follows:

$$\mathcal{H}_{\text{CF}} = B_0^2 C_0^2 + B_0^4 C_0^4 + i B_3^4 (C_3^4 + C_{-3}^4) + B_0^6 C_0^6 + i B_3^6 (C_3^6 + C_{-3}^6) + B_6^6 (C_6^6 + C_{-6}^6). \quad (2)$$

The B_q^p are the crystal field parameters and the C_q^p are the spherical tensor operators. We used the values of the parameter B_q^p reported in Ref. [29]. Matrix elements of J^x, J^y, and J^z in the ground-state doublet $|g_\pm\rangle$ are as follows:

$$\begin{aligned} \langle g_\mp | J^x | g_\pm \rangle &= -1.67 \equiv \frac{\beta}{2}, \\ \langle g_\mp | J^y | g_\pm \rangle &= \pm \frac{\beta}{2} i \\ \langle g_\pm | J^z | g_\pm \rangle &= \mp 0.98 \equiv \mp \frac{\alpha}{2}, \\ \langle g_\pm | J^x | g_\pm \rangle &= \langle g_\pm | J^y | g_\pm \rangle = \langle g_\mp | J^z | g_\pm \rangle = 0, \end{aligned} \quad (3)$$

meaning that the total angular momentum is anisotropic, favoring in plane. Next we inspect anisotropy within the ab plane. The quantization axis is transformed from the z axis to the x axis because the direction of the spin in the order state is along the $x(a)$ axis. Then, the matrix elements of J^x, J^y, and

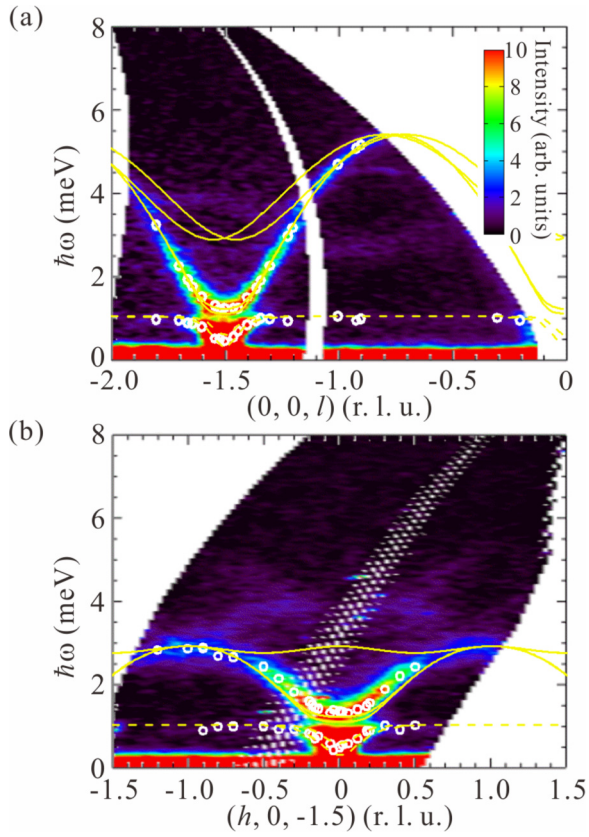

FIG. 4. (Color online) Color maps of the inelastic neutron scattering spectra obtained at HRC, along the (a) l and (b) h directions at 15 K. The open circles are the peak positions extracted Gaussian fits and the curves are the calculated spin-wave dispersions. Fitting curves reasonably reproduce the experimental data. White area in the middle in (a) is the gap between neutron detectors banks.

J^z in the redefined state $|g'_\pm\rangle$ are calculated as follows:

$$\begin{aligned}
\langle g'_\pm| J^x |g'_\pm\rangle &= \mp\frac{\beta}{2},\\
\langle g'_\mp| J^y |g'_\pm\rangle &= \frac{\beta}{2},\\
\langle g'_\mp| J^z |g'_\pm\rangle &= \pm\frac{\alpha}{2}i,\\
\langle g'_\mp| J^x |g'_\pm\rangle &= \langle g'_\pm| J^y |g'_\pm\rangle = \langle g'_\pm| J^z |g'_\pm\rangle = 0.
\end{aligned} \tag{4}$$

The operator $B_6^6(C_6^6 + C_{-6}^6)$ leads to an anisotropy within the ab plane. In order to quantify this, we express the total angular momentum of the Nd^{3+} ion in the ground state doublet as

$$J^x = \frac{\beta}{2}\cos\theta, \quad J^y = \frac{\beta}{2}\sin\theta, \tag{5}$$

where θ is the angle between the a axis and the moment. Thus classical energy of $B_6^6(C_6^6 + C_{-6}^6)$ becomes

$$B_6^6\left(C_6^6 + C_{-6}^6\right) = \frac{\sqrt{231}}{16} B_6^6 \gamma_J \left(\frac{\beta}{2}\right)^6 \cos 6\theta, \tag{6}$$

where $\gamma_J = -3.80 \times 10^{-5}$ is a Stevens' factor. Equation (6) means that the classical energy of the crystal field gives a sixfold anisotropy. Since the sign of the $B_6^6\gamma_J$ is negative, the easy axis is the a axis that is consistent with the magnetic

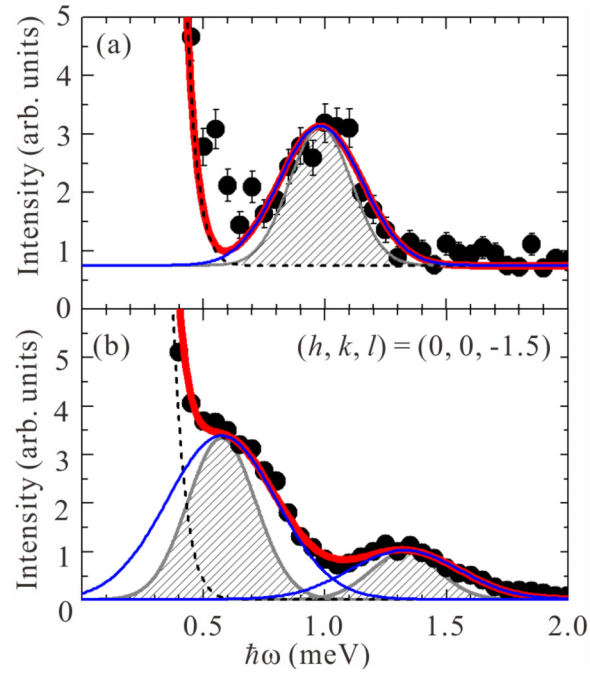

FIG. 5. (Color online) (a) $\hbar\omega$ dependence of the neutron intensity that is obtained by the integration in the $\boldsymbol{q}$ range of $h = [-0.5,0]$ and $l = [-1, -0.7]$. The solid curve is fit to the data by Gaussian functions. (b) Constant-Q scan at $(0,0,-1.5)$. The spectra were integrated in the range of $h = [-0.1,0.1]$ and $l = [-1.6, -1.4]$. The error bars are inside the symbols. The solid curves are fits to the data by Gaussian functions. The gray shaded areas are the energy resolutions: Gaussian functions with full width at half maximum of 0.3 meV.

structure [27]. The magnitude of the calculated anisotropy energy is 65.2 μeV. We effectively include the sixfold anisotropic energy as $-D(J^x)^2$ in the Hamiltonian Eq. (1). The coefficient D is 23.5 μeV, which is defined by the relation:

$$-D\left(\frac{\beta}{2}\right)^2 \equiv \frac{\sqrt{231}}{16} B_6^6 \gamma_J \left(\frac{\beta}{2}\right)^6 \times 2 = 65.2 \ \mu\text{eV}. \tag{7}$$

Next the operators of total angular momentum $\boldsymbol{J}$ are approximated as the operators of pseudospin $s = 1/2$ because the ground state is the Kramers doublet and the degree of freedom is two. The connection between operators of the total angular momentum $\boldsymbol{J}$ and the pseudospin $\boldsymbol{s}$ is determined by the matrix elements Eq. (4). In this approximation the operators of the total angular momentum is redefined as

$$J^x = \beta s^x, \quad J^y = \beta s^y, \quad J^z = \alpha s^z. \tag{8}$$

The Hamiltonian Eq. (1) is, thus, represented by

$$\begin{aligned}
\mathcal{H} = &-\sum_{\text{n.n.}} J_1 \boldsymbol{S}_i \cdot \boldsymbol{S}_j - \sum_{\text{n.n.n.}} J_2 \boldsymbol{S}_i \cdot \boldsymbol{S}_j\\
&- \sum_{\text{n.n.}} J_3 \boldsymbol{S}_i \cdot \begin{pmatrix} \beta s_k^x \\ \beta s_k^y \\ \alpha s_k^z \end{pmatrix} - \sum_k D\left(\beta s_k^x\right)^2.
\end{aligned} \tag{9}$$

We subsequently calculate the spin-wave spectrum of this Hamiltonian using Holstein-Primakoff (HP) transformations.

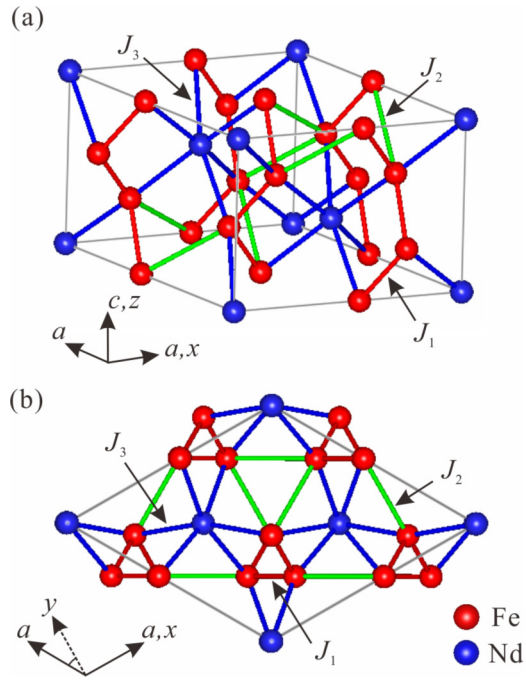

FIG. 6. (Color online) Exchange paths in $NdFe_3(BO_3)_4$. J_1 and J_2 are the nearest and second-nearest-neighbor exchange interactions between the Fe^{3+} moments. J_3 is the nearest-neighbor exchange interaction between the Fe^{3+} and Nd^{3+} moments. The x axis is parallel to the a axis and the z axis is parallel to the c axis. The y axis is vertical to the x and z axis.

The HP transformations of the spin operators of the Fe^{3+} moments and the pseudospin operators of the Nd^{3+} moments are written as

$$S_i^x = S - a_i^\dagger a_i, \tag{10}$$

$$S_i^y = \sqrt{\frac{S}{2}}(a_i^\dagger + a_i), \tag{11}$$

$$S_i^z = -\sqrt{\frac{S}{2}}i(a_i^\dagger - a_i), \tag{12}$$

$$s_i^x = s - b_i^\dagger b_i, \tag{13}$$

$$s_i^y = \sqrt{\frac{s}{2}}(b_i^\dagger + b_i), \tag{14}$$

$$s_i^z = -\sqrt{\frac{s}{2}}i(b_i^\dagger - b_i). \tag{15}$$

The $a_i^\dagger, a_i, b_i^\dagger$ and b_i are bosons operator in each sublattices. The quantization axis is parallel to the $x(a)$ axis. We introduce spatial Fourier transformation via

$$c_i^\dagger(\boldsymbol{q}) = \frac{1}{\sqrt{N}}\sum_{\boldsymbol{r}_i} c_i^\dagger e^{-i\boldsymbol{q}\cdot\boldsymbol{r}_i} \quad (i = 1 \sim 24), \tag{16}$$

where N is the number of unit cells in the system, and $\{c_i\} = \{a_i, b_i\}$ are the bosons operators on each sublattice. By using this notation we obtain

$$\mathcal{H} = \sum_{\boldsymbol{q}}\sum_{ij} A_{ij}(\boldsymbol{q})c_i^\dagger(\boldsymbol{q})c_j(\boldsymbol{q}) + \frac{1}{2}\sum_{ij}[B_{ij}(\boldsymbol{q})c_i^\dagger(\boldsymbol{q})c_j^\dagger(\boldsymbol{q}) + \text{H.c.}]. \tag{17}$$

The eigenvalues of the matrix $(\boldsymbol{A}+\boldsymbol{B})(\boldsymbol{A}-\boldsymbol{B})$ give the squares of the energy of the normal modes [34]:

$$(\boldsymbol{A}+\boldsymbol{B})(\boldsymbol{A}-\boldsymbol{B})\chi_\tau(\boldsymbol{q}) = \{\hbar\omega(\boldsymbol{q})\}^2\chi_\tau(\boldsymbol{q}). \tag{18}$$

The dispersions obtained from this calculation are indicated by the yellow solid curves in Figs. 4(a) and 4(b). In fact we obtained 24 modes of spin waves, but due to the trigonal symmetry of the lattice only eight modes have nonzero spectral weight. The modes at the highest and second-highest energies around the AF zone center, $\boldsymbol{q} = (0,0,-1.5)$, in Fig. 4(a) are twofold degenerated, and the highest-energy mode in Fig. 4(b) is fourfold degenerated. At the zone center, there are two modes at $\hbar\omega = 1.12$ meV and 1.23 meV, and another two modes at $\hbar\omega = 0.32$ meV and 0.61 meV. The 0.32 meV gap is caused by the anisotropy of the Nd^{3+} moment in the ab plane. It vanishes if the D is set to zero. The modes at 1.12 meV and 1.23 meV is the Nd^{3+} level after hybridizing with the dispersive Fe^{3+} spin waves. The small splittings of both modes are due to the easy-plane-type anisotropy of the Nd^{3+} ion, i.e., the effect of $\alpha \neq \beta$. These splittings are the origin of the observed broadenings of the experimental peaks in Fig. 5(b). White circles in Figs. 4(a) and 4(b) are fit by the mean energy of the split modes. χ^2s were calculated for the parameter set with the step sizes of $\delta J_1 = 0.001$ meV, $\delta J_2 = 0.001$ meV, and $\delta J_3 = 0.1$ μeV in the ranges of $|J_1| \leqslant 1$ meV, $|J_2| \leqslant 1$ meV, and $|J_3| \leqslant 0.1$ meV. The obtained parameters set for the minimum χ^2 is listed in Table I. The fit to the data provides excellent agreement with the overall spectrum. It should be noted that the anisotropy gap of about 0.57 meV at the zone center is quantitatively reproduced by using the fixed parameter of $D = 23.5$ μeV obtained from reported value of the parameter B_6^6 [29]. It is revealed that the origin of the in-plane anisotropy is the crystal field of the Nd^{3+} ion.

TABLE I. Parameters obtained by the linear spin-wave calculations.

J_1 (meV)	J_2 (meV)	J_3 (μeV)	D (μeV) (fixed)	χ^2
−0.482	−0.054	7.9	23.5	0.993

V. DISCUSSION

In $RFe_3(BO_3)_4$, the magnitude of the electric polarization by the R^{3+} and Fe^{3+} ions are locally determined by the magnetic moments [22,23]. In the case of $NdFe_3(BO_3)_4$ the existence of the in-plane anisotropy favoring order along the a axis by the Nd^{3+} and/or Fe^{3+} ions is a key to the emergence of the multiferroicity. In the analysis section, uniaxial anisotropy of the Fe^{3+} moments is not considered for simplicity. In this section, we discuss possible magnetic anisotropies in the ab plane of the Fe^{3+} moments.

The conventional origin of anisotropy in Fe^{3+}-based magnets is magnetic-dipole interaction or single-ion anisotropy. The magnetic-dipole interaction between spins $\boldsymbol{S}_i$ and $\boldsymbol{S}_j$ is represented by

$$\mathcal{H}_{\rm dip} = \sum_{i,j} \frac{(g\mu_{\rm B})^2}{r_{ij}^3}\{\boldsymbol{S}_i \cdot \boldsymbol{S}_j - 3(\boldsymbol{S}_i \cdot \boldsymbol{e}_{ij})(\boldsymbol{S}_j \cdot \boldsymbol{e}_{ij})\}, \quad (19)$$

where r_{ij} and $\boldsymbol{e}_{ij}$ are respectively the distance and the unit vector along the bond between i and j. For a collinear in the ab plane, the dipole-interaction energy is independent of the angle to the a axis. This is due to the threefold screw-axis symmetry along the c axis, which also dictates that further neighbor interactions vanish. Thus, the magnetic-dipole interaction is not the origin of the anisotropy in the ab plane.

Next, we consider the single-ion anisotropy of the Fe^{3+} moments. There is only one inequivalent site for the Fe^{3+} ion and the local anisotropy is uniquely determined. Since the screw axis 3_1 or 3_2 is along the Fe^{3+} chain, the FeO_6 octahedra are transformed by $2\pi/3$ rotation around the c axis one another. Therefore, three local coordinates, $\{X_i, Y_i, Z_i\}$, can be defined on the FeO_6 octahedra for the anisotropy. Here $\{i = 1,2,3\}$ are the labels of the Fe^{3+} sites. Since the Fe^{3+} moments are collinear in the ab plane, we discuss the anisotropy only in the ab plane. Then, the general single-ion anisotropy to fourth order in the Fe^{3+} spin-operators is expressed by

$$\begin{aligned}\mathcal{H}_{\rm aniso} = \sum_{i=1,2,3} \big[& a_{x^2}\big(S_i^{X_i}\big)^2 + a_{y^2}\big(S_i^{Y_i}\big)^2 + a_{xy} S_i^{X_i} S_i^{Y_i} \\ & + a_{x^4}\big(S_i^{X_i}\big)^4 + a_{y^4}\big(S_i^{Y_i}\big)^4 + a_{x^2y^2}\big(S_i^{X_i}\big)^2\big(S_i^{Y_i}\big)^2 \\ & + a_{x^3y}\big(S_i^{X_i}\big)^3 S_i^{Y_i} + a_{xy^3} S_i^{X_i}\big(S_i^{Y_i}\big)^3\big]. \end{aligned} \quad (20)$$

The a_{x^2}, a_{y^2}, a_{xy}, a_{x^4}, a_{y^4}, $a_{x^2y^2}$, a_{x^3y}, and a_{xy^3} are independent coefficients. Here we define the the local coordinate $\{X_1, Y_1, Z_1\}$ as the same as the global one $\{x, y, z\}$. Then the relation between the spin operators defined on the local coordinates $\{X_{2,3}, Y_{2,3}, Z_{2,3}\}$ and the those defined on the global one is as follows:

$$\begin{aligned} S_2^{X_2} &= -\frac{1}{2}S_2^x + \frac{\sqrt{3}}{2}S_2^y, \quad S_2^{Y_2} = -\frac{\sqrt{3}}{2}S_2^x - \frac{1}{2}S_2^y, \\ S_2^{Z_2} &= S_2^z, \end{aligned} \quad (21)$$

$$\begin{aligned} S_3^{X_3} &= -\frac{1}{2}S_3^x - \frac{\sqrt{3}}{2}S_3^y, \quad S_3^{Y_3} = \frac{\sqrt{3}}{2}S_3^x - \frac{1}{2}S_3^y, \\ S_3^{Z_3} &= S_3^z, \end{aligned} \quad (22)$$

where the x axis is parallel to the crystallographic a axis and the z axis is parallel to the c axis. These relations are substituted into Eq. (20) to express the single-ion anisotropy in global coordinates. Hereafter we classically calculate the anisotropy energy of the collinear AF structure in the ab plane. The Fe^{3+} spin operators are classically expressed by

$$\begin{aligned} \big(S_1^x, S_1^y, S_1^z\big) &= (S\cos\theta, S\sin\theta, 0), \\ \big(S_2^x, S_2^y, S_2^z\big) &= (-S\cos\theta, -S\sin\theta, 0), \\ \big(S_3^x, S_3^y, S_3^z\big) &= (S\cos\theta, S\sin\theta, 0), \end{aligned} \quad (23)$$

where the Fe^{3+} moments are functions of the angle θ between the a axis and the Fe^{3+} moments in the ab plane. It is found that energy is independent on the angle θ. Consequently, the single-ion anisotropy does not give the anisotropy of the Fe^{3+} moment in the ab plane.

In the multiferroic compound $Ba_2CoGe_2O_7$ with the metal-ligand hybridization mechanism, it was reported that an interaction between the electric polarization determines the magnetic anisotropy in the easy plane [35]. We hence consider the electric-polarization interaction in $NdFe_3(BO_3)_4$ using the mechanism, where the local electric-polarization at the Fe^{3+} site is expressed by $\boldsymbol{p}_i = t\sum_l (\boldsymbol{e}_l \cdot \boldsymbol{S}_i)^2 \boldsymbol{e}_l$. Here $\boldsymbol{e}_l$ is a unit vector along the bond to ligands (in this case oxygen), and t is a coupling constant related with the metal-ligand hybridization and the spin-orbit interaction. The polarization interaction is represented by $J_{\rm p}\sum_{ij} \boldsymbol{p}_i \cdot \boldsymbol{p}_j$. $J_{\rm p}$ is the ferroelectric coupling constant between the electric polarizations $\boldsymbol{p}_i$. The energy of the polarization interaction was calculated as a function of angle between the a axis and the Fe^{3+} moments in the ab plane. It was then found that the energy is independent of the direction of the Fe^{3+} moments in the ab plane. Thus, the polarization interaction does not cause the uniaxial anisotropy in the ab plane.

Accordingly, at the Fe^{3+} site the conventional sources of magnetic anisotropy such as the magnetic-dipole interaction and single-ion anisotropy, and the polarization interaction do not lead to the a-axis anisotropy under the restriction that the crystal symmetry is preserved. This means that the Fe^{3+} moment does not have any uniaxial anisotropy in the ab plane unless there is any disorder, which breaks the threefold rotation symmetry, for instance, lattice distortion, and quantum and thermal fluctuations [36,37]. The direction of the Fe^{3+} moment, therefore, is determined by the anisotropy of the Nd^{3+} moment through the f-d coupling. It can be said that the magnetic anisotropy of the Nd^{3+} moments by the crystal field drives the multiferroicity in $NdFe_3(BO_3)_4$.

The multiferroic mechanism of $RFe_3(BO_3)_4$ is the spin-dependent metal-ligand hybridization model [22,23] where the relation between the electric polarization and the magnetic moment is locally determined by the symmetry of O^{2-} ions around the magnetic ion. In a collinear magnetic structure the local magnetic anisotropy is a casting vote in the determination of the magnetic structure, and, consequently, in the determination of the electric polarization as well. In $NdFe_3(BO_3)_4$ the crystal field of the Nd^{3+} ion is revealed to be the origin of the magnetic anisotropy, which determines the bulk structure of multiferroics. This is in contrast with the multiferroic materials of which the mechanism is the spin current model [11,12], where the relation is determined by the geometry of neighboring magnetic moments.

VI. CONCLUSION

We performed INS measurements to explore the magnetic excitations, to establish the underlying Hamiltonian, and to reveal the detailed nature of hybridization between the $4f$ and $3d$ magnetism in $NdFe_3(^{11}BO_3)_4$. Overall spectra are reasonably reproduced by spin-wave calculation including spin interaction in the framework of weakly coupled Fe^{3+} chains, f-d coupling, and single-ion anisotropy derived from the Nd^{3+} crystal

field. Hybridization between the $4f$ and $3d$ magnetism is probed as anticrossing of the Nd- and Fe-centered excitations. The anisotropy gap observed at the AF zone center is explained by the crystal field of the Nd^{3+} ion in the quantitative level. Magnetic anisotropy of the Fe^{3+} ion allowed in the present crystal structure is small so that it cannot be dominant. Combination of the measurements and calculations revealed that the hybridization between $4f$ and $3d$ magnetism propagates the local magnetic anisotropy of the Nd^{3+} ion to the Fe^{3+} network, resulting in the bulk magnetic structure. In the multiferroics of the spin-dependent metal-ligand hybridization type, the local magnetic anisotropy controls the electric polarization, meaning that the local symmetry of the rare-earth ion is a driving force for the nonlocal multiferroicity in $NdFe_3(BO_3)_4$.

ACKNOWLEDGMENTS

We thank H. Matsuda, and K. Asoh for their contribution to the single crystal growth. The neutron scattering experiment was approved by the Neutron Scattering Program Advisory Committee of IMSS, KEK (Proposals No. 2013S01 and No. 2014S01) and ISSP. H.M.R. gratefully thanks ISSP for the hospitality, and support from the Swiss National Science Foundation and its Sinergia network Mott Physics Beyond the Heisenberg Model (MPBH). This work was supported by JSPS KAKENHI Grant in Aid for Scientific Research (B) Grant No. 24340077. S.H. was supported by the Japan Society for the Promotion of Science through the Program for Leading Graduate Schools (MERIT).

[1] T. Kimura, T. Goto, H. Shintani, K. Ishizaka, T. Arima, and Y. Tokura, Nature (London) **426**, 55 (2003).
[2] T. Goto, T. Kimura, G. Lawes, A. P. Ramirez, and Y. Tokura, Phys. Rev. Lett. **92**, 257201 (2004).
[3] T. Kimura, G. Lawes, and A. P. Ramirez, Phys. Rev. Lett. **94**, 137201 (2005).
[4] G. Lawes, A. B. Harris, T. Kimura, N. Rogado, R. J. Cava, A. Aharony, O. Entin-Wohlman, T. Yildirim, M. Kenzelmann, C. Broholm, and A. P. Ramirez, Phys. Rev. Lett. **95**, 087205 (2005).
[5] Y. Yamasaki, S. Miyasaka, Y. Kaneko, J.-P. He, T. Arima, and Y. Tokura, Phys. Rev. Lett. **96**, 207204 (2006).
[6] K. Taniguchi, N. Abe, T. Takenobu, Y. Iwasa, and T. Arima, Phys. Rev. Lett. **97**, 097203 (2006).
[7] T. Kimura, J. C. Lashley, and A. P. Ramirez, Phys. Rev. B **73**, 220401 (2006).
[8] S. Park, Y. J. Choi, C. L. Zhang, and S-W. Cheong, Phys. Rev. Lett. **98**, 057601 (2007).
[9] Y. Naito, K. Sato, Y. Yasui, Y. Kobayashi, Y. Kobayashi, and M. Sato, J. Phys. Soc. Jpn. **76**, 023708 (2007).
[10] H. Murakawa, Y. Onose, S. Miyahara, N. Furukawa, and Y. Tokura, Phys. Rev. Lett. **105**, 137202 (2010).
[11] H. Katsura, N. Nagaosa, and A. V. Balatsky, Phys. Rev. Lett. **95**, 057205 (2005).
[12] M. Mostovoy, Phys. Rev. Lett. **96**, 067601 (2006).
[13] I. A. Sergienko and E. Dagotto, Phys. Rev. B **73**, 094434 (2006).
[14] C. Jia, S. Onoda, N. Nagaosa, and J. H. Han, Phys. Rev. B **76**, 144424 (2007).
[15] T. Arima, J. Phys. Soc. Jpn. **76**, 073702 (2007).
[16] A. K. Zvezdin, S. S. Krotov, A. M. Kadomtseva, G. P. Vorob'ev, Yu. F. Popov, A. P. Pyatakov, L. N. Bezmaternykh, and E. A. Popova, JETP Lett. **81**, 272 (2005).
[17] A. K. Zvezdin, G. P. Vorob'ev, A. M. Kadomtseva, Yu. F. Popov, A. P. Pyatakov, L. N. Bezmaternykh, A. V. Kuvardin, and E. A. Popova, JETP Lett. **83**, 509 (2006).
[18] A. M. Kadomtseva, A. K. Zvezdin, A. P. Pyatakov, A. V. Kuvardin, G. P. Vorob'ev, Yu. F. Popov, and L. N. Bezmaternykh, JETP **105**, 116 (2007).
[19] A. K. Zvezdin, A. M. Kadomtseva, Yu. F. Popov, G. P. Vorob'ev, A. P. Pyatakov, V. Yu. Ivanov, A. M. Kuz'menko, A. A. Mukhin, L. N. Bezmaternykh, and I. A. Gudim, JETP **109**, 68 (2009).
[20] A. M. Kadomtseva, Yu. F. Popov, G. P. Vorob'ev, A. P. Pyatakov, S. S. Krotov, and K. I. Kamilov, Low Temp. Phys. **36**, 511 (2010).
[21] U. Adem, L. Wang, D. Fausti, W. Schottenhamel, P. H. M. van Loosdrecht, A. Vasiliev, L. N. Bezmaternykh, B. Büchner, C. Hess, and R. Klingeler, Phys. Rev. B **82**, 064406 (2010).
[22] A. I. Popov, D. I. Plokhov, and A. K. Zvezdin, Phys. Rev. B **87**, 024413 (2013).
[23] T. Kurumaji, K. Ohgushi, and Y. Tokura, Phys. Rev. B **89**, 195126 (2014).
[24] J. A. Campá, C. Cascales, E. Gutiérrez-Puebla, M. A. Monge, I. Rasines, and C. Ruíz-Valero, Chem. Mater. **9**, 237 (1997).
[25] N. Tristan, R. Klingeler, C. Hess, B. Büchner, E. Popova, I. A. Gudim, and L. N. Bezmaternykh, J. Magn. Magn. Mater. **316**, e621 (2007).
[26] P. Fischer, V. Pomjakushin, D. Sheptyakov, L. Keller M. Janoschek, B. Roessli, J. Schefer, G. Petrakovskii, L. Bezmaternikh, V. Temerov, and D. Velikonov, J. Phys.: Condens. Matter **18**, 7975 (2006)
[27] M. Janoschek, P. Fischer, J. Schefer, B. Roessli, V. Pomjakushin, M. Meven, V. Petricek, G. Petrakovskii, and L. Bezmaternikh, Phys. Rev. B **81**, 094429 (2010).
[28] A. M. Kuz'menko, A. A. Mukhin, V. Yu. Ivanov, A. M. Kadomtseva, and L. N. Bezmaternykh, JETP Lett. **94**, 294 (2011).
[29] M. N. Popova, E. P. Chukalina, T. N. Stanislavchuk, B. Z. Malkin, A. R. Zakirov, E. Antic-Fidancev, E. A. Popova, L. N. Bezmaternykh, and V. L. Temerov, Phys. Rev. B **75**, 224435 (2007).
[30] L. N. Bezmaternykh, S. A. Kharlamova, and V. L. Temerov, Crystallogr. Rep. **49**, 855 (2004).
[31] S. Itoh, T. Yokoo, S. Satoh, S. Yano, D. Kawana, J. Suzuki, and T. J. Sato, Nucl. Instr. Meth. Phys. Res. A **631**, 90 (2011).
[32] S. Yano, S. Itoh, S. Satoh, T. Yokoo, D. Kawana, and T. J. Sato, Nucl. Instr. Meth. Phys. Res. A **654**, 421 (2011).

[33] S. Itoh, T. Yokoo, D. Kawana, H. Yoshizawa, T. Masuda, M. Soda, T. J. Sato, S. Satoh, M. Sakaguchi, and S. Muto, J. Phys. Soc. Jpn. **82**, SA033 (2013).

[34] R. Sachidanandam, T. Yildirim, A. B. Harris, A. Aharony, and O. Entin-Wohlman, Phys. Rev. B **56**, 260 (1997).

[35] M. Soda, M. Matsumoto, M. Mänsson, S. Ohira-Kawamura, K. Nakajima, R. Shiina, and T. Masuda, Phys. Rev. Lett. **112**, 127205 (2014).

[36] E. F. Shender, Ż. Ėksp. Teor. Fiz. **83**, 326 (1082) [Sov. Phys. JETP **56**, 178 (1982)].

[37] C. L. Henley, Phys. Rev. Lett. **73**, 2788 (1994).